

# Encapsulating Pt Nanoparticles inside a Derived Two-Dimensional Metal–Organic Frameworks for the Enhancement of Catalytic Activity

Wei Wu, Zeyi Zhang, Zhao Lei, Xiaoyue Wang, Yangyang Tan, Niancai Cheng,\* and Xueliang Sun\*



Cite This: *ACS Appl. Mater. Interfaces* 2020, 12, 10359–10368



Read Online

ACCESS |



Metrics & More

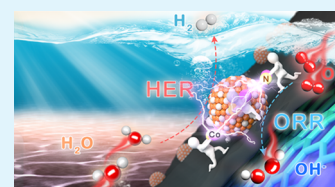


Article Recommendations



Supporting Information

**ABSTRACT:** The development of highly active and stable electrocatalysts toward oxygen reduction reaction (ORR) and hydrogen evolution reaction (HER) is a key for commercial application of fuel cells and water splitting. Here, we report a highly active and stable Pt nanoparticles (NPs) encapsulated in ultrathin two-dimensional (2D) carbon layers derived from the ultrathin 2D metal–organic framework precursor (ZIF-67). Electrochemical tests reveal that our approach not only stabilized Pt NPs successfully but also boosted Pt activities toward ORR and HER. We found that our Pt catalysts encapsulated in ultrathin 2D carbon layers exhibited an ORR activity of 5.9 and 12 times greater than those of the commercial Pt/C and Pt/RGO without 2D carbon layer protection. Our encapsulated Pt catalysts also show more than nine times higher stability than those of Pt/C catalysts. In addition to ORR, our novel encapsulated Pt catalysts display an extraordinary stability and activity toward HER, with a lower overpotential (14.3 mV in acidic media and 37.2 mV in alkaline media) at a current density of 10 mA cm<sup>-2</sup> than Pt/C catalysts (23.1 mV in acidic media and 92.1 mV in alkaline media). The enhanced electrochemical activities and stability of our encapsulated Pt catalysts are attributed to the synergistic effect of Pt-based NPs and ultrathin 2D carbon layers derived from ZIF-67 with enriched active sites Co–N<sub>x</sub>. First-principles simulations reveal that the synergistic catalysis of Pt-based NPs and Co–N<sub>x</sub> derived from ZIF-67 improves the activity for ORR and HER.



**KEYWORDS:** synergistic catalysis, encapsulated nanoparticles, Pt catalysts, oxygen reduction reaction, hydrogen evolution reaction

## 1. INTRODUCTION

Platinum (Pt)-based catalysts are believed as the most efficient electrocatalysts in many important clean energy processes such as hydrogen oxidation reaction and oxygen reduction reaction (ORR) in fuel cells and hydrogen evolution reaction (HER) in electrochemical water splitting.<sup>1–6</sup> To maximize the Pt utilization efficiency and decrease the cost of catalysts, Pt nanoparticles (NPs) or clusters, even atoms, were deposited on a support to improve the catalytic performance. However, instability is still one of the major challenges for supported Pt NPs in practical applications because NPs easily aggregate and form larger particles to minimize the surface energy, resulting in a serious loss of the catalytic activity.<sup>7–9</sup> Moreover, supported Pt NPs often suffer from performance degradation due to the dissolution, detachment, or aggregation of Pt NPs on supports in harsh environments such as high-potential, concentrated acid and alkaline media in practical applications.<sup>2,10,11</sup>

To address the above challenges associated with supported Pt catalysts, one of the best strategies is surface protection of individual metal nanoparticles encapsulated into an ultrathin layer that can effectively suppress the leaching, detachment, and agglomeration of metal NPs on supports, leading to the enhancement of activity and stability of metal NPs.<sup>10</sup> So far, various protective layers such as carbon,<sup>12–14</sup> metal oxides,<sup>15–17</sup> and polymers<sup>18,19</sup> have been utilized to stabilize

NPs, which show enhanced stability in comparison with the unprotected counterparts. Especially, it is known that carbon layers are the good protective layers to stabilize the small NPs due to the high conductivity and excellent chemical stability in acid and alkaline media. The encapsulated NPs with carbon layers<sup>12,20,21</sup> exhibited an enhanced stability in comparison with unprotected NPs catalysts because carbon layers can not only inhibit NPs from migrating, agglomerating, and detaching but also alleviate the leaching of NPs dissolution. N-doped carbon layers<sup>14,22,23</sup> also were used as protective layers to stabilize the metal NPs, which increase the activity in addition to the enhancement in the stability due to N–C also acting as an active site.

The precise controlled thickness of protective layers plays a vital role in the performance of the surface protection of individual metal nanoparticles because too thin layers cannot effectively protect the metal NPs, while too thick ones lead to a decrease in catalytic activity resulting from mass transfer resistance.<sup>24,25</sup> In addition, the precise structure design of the protective layers such as nanowires,<sup>16,26,27</sup> nanobowls,<sup>28</sup>

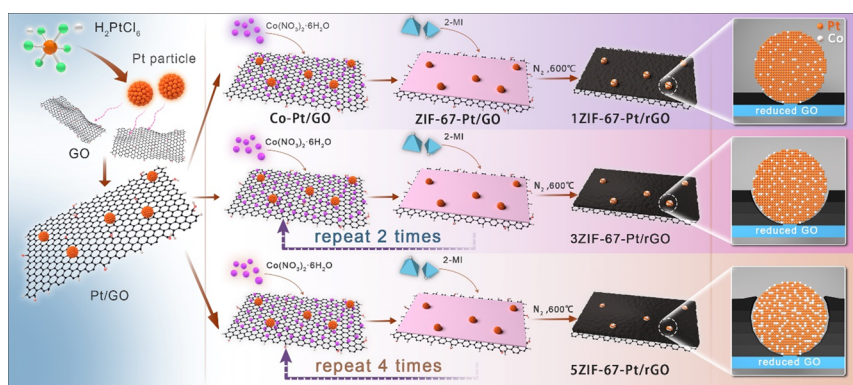
**Received:** November 15, 2019

**Accepted:** February 5, 2020

**Published:** February 5, 2020



**Scheme 1. Schematic of the Strategy for the Synthesis of Pt NPs Encapsulated in Ultrathin 2D Carbon Layers Derived from Ultrathin 2D MOFs Layers**



nanocages,<sup>15</sup> and nanotraps<sup>29</sup> with open nanochannels is crucial for high activity of encapsulated metal NPs because those nanochannels could not only highly expose the active sites but also facilitate the mass transfer for the reactants and products and eliminate the deactivation of catalysts by lowering the diffusion. Recently, metal–organic frameworks (MOFs) have been indicating promising potential to become a new generation of protective layer materials for encapsulating NPs because cavities in MOFs could favor the mass transfer in comparison with conventional porous materials.<sup>30–32</sup> The most reported method to encapsulate metal NPs into MOFs is the growth of the granular MOF crystal shell on the surface of metal NPs through mixing MOF precursors of both metal ions and organic linkers;<sup>33–35</sup> however, the precise control of the shell thickness and open nanochannels of MOF layers is still a challenge. Besides the challenges associated with instability of Pt catalysts, another major problem for Pt electrocatalysts is a high cost due to expensive and scarce Pt.<sup>36</sup> Therefore, it is extremely desirable to further improve the activity and stability of the Pt-based catalysts for their widespread application.

In this work, taking advantage of MOFs, we propose a strategy to design highly active and stable catalysts through encapsulating Pt NPs in ultrathin 2D cobalt MOF (ZIF-67)-derived carbon layers. The precise control of ultrathin 2D carbon layers plays a vital role in achieving highly active and stable encapsulated Pt catalysts, in which ultrathin 2D carbon layers not only suppress the growth and leaching of metal NPs resulting in high stability but also solve the diffusion barriers for the reactants and products without lowering the activity of catalysts. An outline of the synthetic strategy for the Pt encapsulated in ultrathin 2D carbon layers is illustrated in Scheme 1. The uniform Pt NPs were first deposited on the graphene oxides (GOs), and then the ultrathin 2D ZIF-67 using 2-methylimidazole and cobalt(II) nitrate hexahydrate as precursors grew around Pt NPs on the surface of GO. In this work, we precisely control the thickness of the ultrathin 2D MOFs through a step-by-step method.<sup>37</sup> After thermal decomposition of ultrathin 2D ZIF-67 precursors, the Pt NPs encapsulated in ultrathin 2D carbon layers derived from ZIF-67 precursors show high stability with enhanced activity toward ORR and HER due to the synergistic effect between Pt catalysts and the active sites (Co–N<sub>x</sub>) on ZIF-67-derived ultrathin 2D carbon layers.

## 2. RESULTS AND DISCUSSION

GO was regarded as a good adsorption material for heavy metal ions due to its excellent adsorption performance.<sup>38</sup> GO can effectively bind a metal ion through sharing an electron pair resulting from the carboxylate groups such as –COOH and –C=O.<sup>39</sup> Taking advantage of the excellent adsorption performance of graphene oxide, cobalt ions could be anchored to the GO surface through the strong coordination of carboxylate groups with metal cations and subsequently form 2D MOFs by the assembly of adsorbed metal cations with organic linkers. In order to precisely control the thickness of 2D ZIF-67, we adopted the step-by-step method<sup>37</sup> to grow 2D ZIF-67 on the surface of GO. The typical procedure includes the following steps: (1) the adsorption of cobalt ions on GO in methanol solution, (2) the collection of graphene oxide-adsorbed cobalt ions through removal of the excess cobalt precursor in solution, (3) the reaction of 2-methylimidazole with cobalt ions adsorbed to form ZIF-67 on graphene oxides, and (4) the collection of the mixture of ZIF-67 on graphene oxides by removing the excess 2-methylimidazole. One cycle of growth of ZIF-67 layers on GO was achieved. Through tuning the number of the above procedure, the thickness of 2D ZIF-67 on GO can be precisely controlled. We first investigated the thickness of porous N-doped carbon layers derived from ZIF-67 on GO using an atomic force microscope (AFM). As shown in Figure S1, the thickness of porous N-doped carbon layers derived from one cycle ZIF-67-coated GO is ~1.8 nm. The thickness of porous N-doped carbon layers derived from ZIF-67 increased with the increase in cycles of ZIF-67 coating GO. The thicknesses of carbon layers derived from three and five cycles ZIF-67-coated GO were about 4.0 and 5.7 nm, respectively.

To avoid destroying the nature of oxygen-containing functional groups on GO, we first prepared Pt NPs using a modified polyol method<sup>40,41</sup> followed by depositing Pt NPs on GO at room temperature. The Pt NPs with an average particle size of 2.1 nm in diameter were uniformly supported on the surface of GO (Figure S2). As shown in Scheme 1, the Pt encapsulated in ultrathin 2D ZIF-67 is formed by growing ZIF-67 around Pt on the surface of GO. After the pyrolysis of Pt encapsulated in ultrathin 2D MOF layers, we found that the ultrathin 2D carbon layers as protective layers can effectively prevent Pt sintering and aggregation. As shown in Figure S3, the average size of Pt NPs on graphene without MOF protective layers shows distinct aggregation and an increase from 2.1 to 5.3 nm with a large size range annealing at 600 °C

for 3 h at an  $N_2$  atmosphere. In contrast, the average size of Pt NPs with one cycle of ZIF-67 protective layer increased to 4.2 nm (Figure S3b). The average size of Pt NPs in diameter increased slightly to 3.1 and 2.9 nm for 3ZIF-67-Pt/RGO and 5ZIF-67-Pt/RGO, respectively (Figure 1 and Figure S3). More

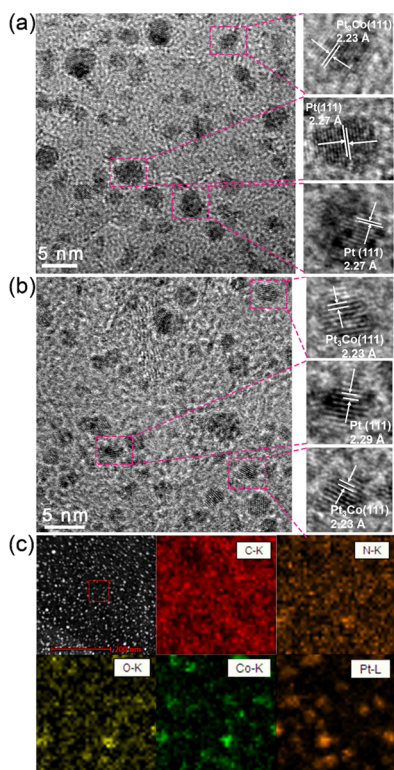


**Figure 1.** High-resolution TEM image of (a) 3ZIF-67-Pt/RGO and (b) 5ZIF-67-Pt/RGO treated at 600 °C for 3 h at an  $N_2$  atmosphere. (c) EDX mapping of 3ZIF-67-Pt/RGO.

importantly, we found that the thickness of ultrathin carbon layers derived from ZIF-67 increase with the cycle. For 1ZIF-67-Pt/RGO, the carbon layers were not clearly observed because the thickness was too thin. It is obvious that ultrathin carbon layers derived from ZIF-67 formed around the Pt NPs for 3ZIF-67-Pt/RGO (Figure 1a). The thickness of the carbon layers of 5ZIF-67-Pt/RGO is higher than that of 3ZIF-67-Pt/RGO. However, compared with 3ZIF-67-Pt/RGO, it is observed that some Pt surface is covered by the derived carbon layers for 5ZIF-67-Pt/RGO resulting from the higher

thickness of ZIF-67 and epitaxial growth (Figure 1b). Those covered Pt surface may result in the loss of activity due to the blocking of the Pt active site covered by protective layers. The energy-dispersive X-ray spectroscopy (EDS) mapping reveals that elements Pt, Co, and N were homogeneously distributed in 3ZIF-67-Pt/RGO (Figure 1c). In addition, some  $Pt_3Co$  NPs were observed in 3ZIF-67-Pt/RGO and 5ZIF-67-Pt/RGO due to the incorporation of the Co into the Pt NPs at high temperature, which proved to improve the activity of Pt NPs.<sup>42–44</sup> The stabilization effect of MOF protective layers for Pt NPs was further confirmed by X-ray diffraction (XRD), as shown in Figure 2a, which showed broader peaks for Pt NPs encapsulated in ultrathin 2D carbon layers than with Pt/RGO without carbon protective layers. In addition, the XRD results showed that the Pt/RGO is a typical face-centered cubic (fcc) structure. Compared with the Pt/RGO, the ZIF-67-Pt/RGO show a Pt–Co peak in addition to the Pt peak, indicating that partial Pt NPs is gradually converted to a Pt–Co alloy through the incorporation of the Co into the Pt fcc structure at high temperature.<sup>45</sup> A Pt alloy with transition metals is proved to enhance the Pt activity.<sup>46,47</sup> X-ray photoelectron spectroscopy (XPS) further confirmed this transformation from partial Pt NPs to a Pt–Co alloy. As shown in Figure 2b, the deconvolution of the Pt 4f spectrum indicates four peaks that are located at about 70.9 and 74.2 eV assigned to the  $4f_{7/2}$  and  $4f_{5/2}$  of metallic Pt and 71.9 and 75.3 eV attributed to the  $4f_{7/2}$  and  $4f_{5/2}$  of  $Pt^{2+}$ . As shown in Table S1, the Pt 4f binding energy of 3ZIF-67-Pt/RGO and 5ZIF-67-Pt/RGO shows a  $\sim 0.4$  eV positive energy shift in comparison with the Pt/RGO, resulting from the formation of the Pt–Co alloy.<sup>43</sup> Three types of nitrogen species for the 5ZIF-67-Pt/RGO sample could be observed in the high-resolution XPS N 1s spectra (Figure S5a): pyridinic N ( $\sim 398.3$  eV), graphitic N ( $\sim 401.0$  eV), and Co– $N_x$  ( $\sim 399.5$  eV).<sup>48</sup> In addition to cobalt, Co XPS further shows that the cobalt exists as Co– $N_x$  in 5ZIF-67-Pt/RGO (Figure S5b).<sup>49,50</sup> This finding is in accordance with the previous studies that showed the formation of Co– $N_x$  species in ZIF-67-derived carbon nanomaterials.<sup>51,52</sup> XPS did not detect the cobalt signal because of the low content of cobalt in 1ZIF-67-Pt/RGO and 3ZIF-67-Pt/RGO (Figure S4).

We first investigate the effect of different ZIF-67 growth cycles on the electrochemical active surface area (ECSA) and ORR activity of encapsulated Pt NPs. As shown in Figure S6, the ECSA of 3ZIF-67-Pt/RGO is measured to be  $55.8 \text{ m}^2 \text{ g}^{-1}$ , which is larger than those of 1ZIF-67-Pt/RGO ( $36.1 \text{ m}^2 \text{ g}^{-1}$ ) and 5ZIF-67-Pt/RGO ( $46.7 \text{ m}^2 \text{ g}^{-1}$ ). Compared with 3ZIF-67-

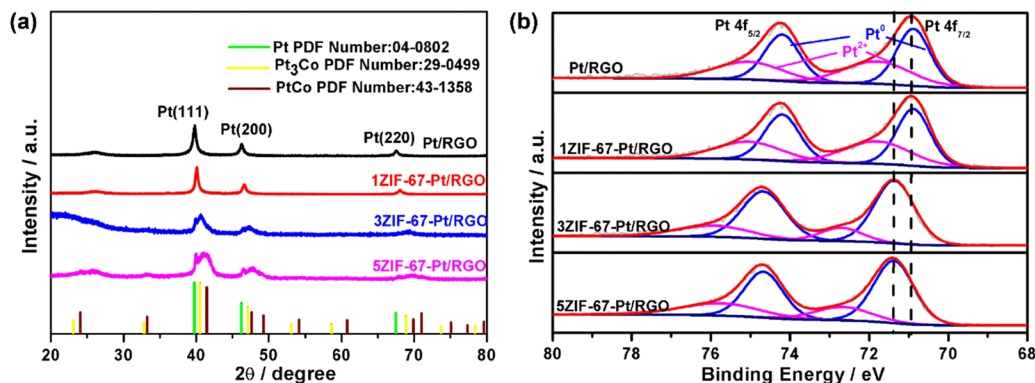


**Figure 2.** (a) XRD patterns and (b) XPS Pt 4f spectra of Pt/RGO and Pt/RGO with different cycles of ZIF-67.

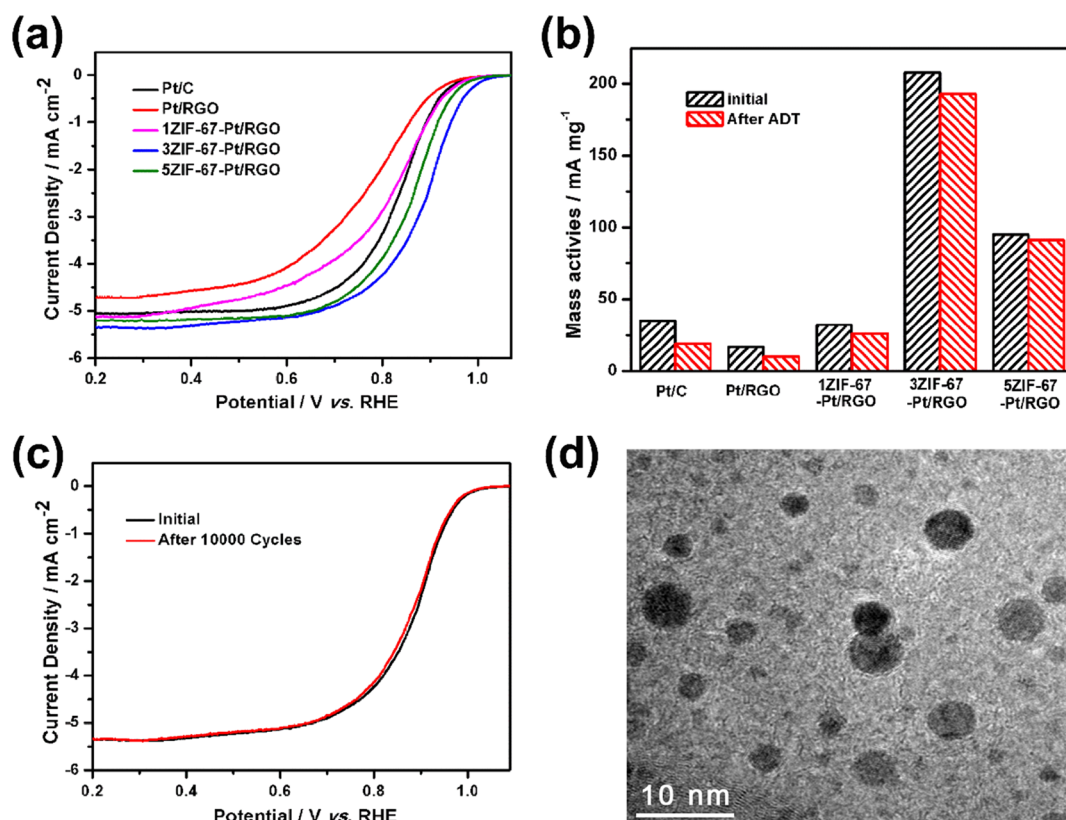


**Figure 3.** (a) ORR polarization curves for Pt/C, Pt/RGO, and Pt/RGO with different cycles of ZIF-67 in O<sub>2</sub>-saturated 0.5 M H<sub>2</sub>SO<sub>4</sub> at room temperature with a rotation rate of 1600 rpm and a sweep rate of 10 mV s<sup>-1</sup>. (b) Mass activity at 0.9 V (vs RHE) for Pt/C, Pt/RGO, and Pt/RGO with different cycles of ZIF-67 before and after ADT. (c) Durability tests for 3ZIF-67-Pt/RGO in O<sub>2</sub>-saturated 0.5 M H<sub>2</sub>SO<sub>4</sub> solution at room temperature. (d) HRTEM image of 3ZIF-67-Pt/RGO after ADT.

Pt/RGO, 1ZIF-67-Pt/RGO has lower ECSA due to the larger size of Pt NPs, which is in good agreement with the result of TEM (Figure S3 and Figure 1). The lower ECSA on 5ZIF-67-Pt/RGO is attributed to some Pt surface covered by ZIF-67, in accordance with the observation from TEM (Figure 1). This finding suggests that it is very important to control the cycle of ZIF-67 for high-performance Pt NPs encapsulated in ultrathin 2D carbon layers derived from ZIF-67. According to ORR polarization curves in Figure 3, the ORR activity of different catalysts increases in the order Pt/RGO < 1ZIF-67-Pt/RGO < Pt/C < 5ZIF-67-Pt/RGO < 3ZIF-67-Pt/RGO in terms of the half-wave potential. Pt/RGO has the lowest ORR activity because of large Pt particles resulting from the treatment in high temperature. 3ZIF-67-Pt/RGO has higher ORR activity than the 5ZIF-67-Pt/RGO (Figure 3a), which is mainly because of some Pt surface covered by the carbon layers derived from the ZIF-67 in 5ZIF-67-Pt/RGO (Figure 1b). Those ORR performances are consistent with the analysis of TEM images. Therefore, it is very important to optimize the structure of the protecting layers for encapsulated metal NPs, which will lead to the highest exposed active site of NPs and promote the mass transfer.<sup>15</sup> As shown in Figure 3b, the mass activity of 3ZIF-67-Pt/RGO is 208 mA·mg<sup>-1</sup>, which is 5.9 times and 12 times better than those of commercial Pt/C catalyst (35 mA·mg<sup>-1</sup>) and Pt/RGO (17 mA·mg<sup>-1</sup>), respectively. The 3ZIF-67-Pt/RGO catalyst also shows higher ORR activity than the PtCo alloy prepared by a typical wet chemical method (Figure S7a). In addition, the 3ZIF-67-Pt/RGO catalyst indicates higher ORR activity than Pt NPs encapsulated in ultrathin 2D carbon layers derived from the

three cycles of ZIF-8 precursors (Figure S7b). Besides, carbonized ZIF-67 on GO without Pt NPs shows poor ORR activity (Figure S7c). Hence, the enhanced ORR activity is probably due to the synergistic catalysis of Pt-based NPs and Co-N<sub>x</sub> derived from ZIF-67.<sup>53,54</sup> As reported, the Co-N<sub>x</sub> derived from ZIF-67 has been widely recognized as active sites for ORR in both acidic and alkaline solutions.<sup>55,56</sup> Accelerated durability tests (ADT) were conducted to study the effect of stabilization of ultrathin carbon layers derived from ZIF-67 by cycling the potentials between 0.6 and 1.0 V vs RHE in 0.5 M H<sub>2</sub>SO<sub>4</sub> using RDE. It was reported that the performance degradation of supported Pt NPs results from the dissolution, migration, and agglomeration of NPs in a cycling potential range between 0.6 and 1.0 V vs RHE.<sup>46</sup> As shown in Figure 3b,c and Figure S8, ultrathin carbon layers derived from ZIF-67 can effectively enhance the stability of Pt NPs. After ADT, 3ZIF-67-Pt/RGO and 5ZIF-67-Pt/RGO catalysts lost only about 7 and 5% of their initial Pt ORR mass activities, respectively; whereas, Pt/C and Pt/RGO catalysts decreased by 46 and 40% of their initial mass activities, respectively. After 10,000 cycles, the mass activity of 3ZIF-67-Pt/RGO is 193 mA·mg<sup>-1</sup>, which is more than 10 times higher than that of the Pt/C catalyst (19 mA·mg<sup>-1</sup>). No significant aggregation or morphology change was observed for the 3ZIF-67-Pt/RGO catalyst, generally maintaining its initial size of Pt NPs after long-term potential cycling (Figure 3d and Figure S9), while the size of the Pt NPs in the Pt/C catalyst significantly increased from 3.6 to 7.8 nm, as shown in Figure S10. This finding suggested that the 2D ultrathin carbon layers derived

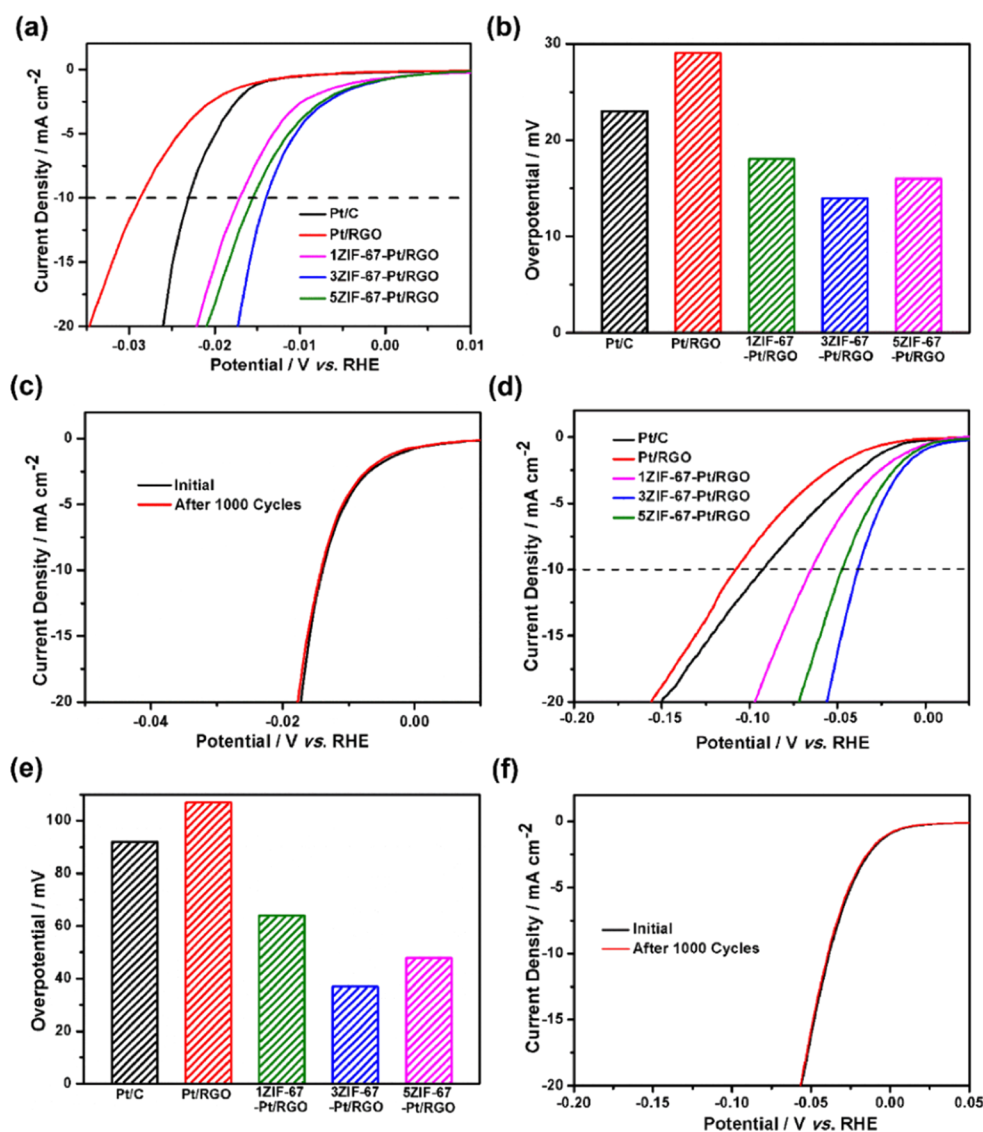


**Figure 4.** (a) Polarization curves and (b) overpotential at  $10 \text{ mA cm}^{-2}$  of Pt/C, Pt/RGO, and Pt/RGO with different cycles of ZIF-67 in  $0.5 \text{ M H}_2\text{SO}_4$  at a scan rate of  $5 \text{ mV}\cdot\text{s}^{-1}$  with a rotation rate of  $1600 \text{ rpm}$ . (c) Polarization curves recorded for 3ZIF-67-Pt/RGO before and after 1000 CV cycles in  $0.5 \text{ M H}_2\text{SO}_4$  (cycling sweep range:  $-0.04 \text{ V}$  to  $0.36 \text{ V}$  vs RHE). (d) Polarization curves and (e) overpotential at  $10 \text{ mA cm}^{-2}$  of Pt/C, Pt/RGO, and Pt/RGO with different cycles of ZIF-67 in  $1 \text{ M KOH}$  at a scan rate of  $5 \text{ mV}\cdot\text{s}^{-1}$  with a rotation rate of  $1600 \text{ rpm}$ . (f) Polarization curves recorded for 3ZIF-67-Pt/RGO before and after 1000 CV cycles in  $1 \text{ M KOH}$  (cycling sweep range:  $-0.15 \text{ V}$  to  $0.25 \text{ V}$  vs RHE).

from ZIF-67 can effectively stabilize the encapsulated Pt NPs and protect Pt NPs from agglomeration and coarsening.

We also investigated the HER electrocatalytic activity of Pt catalysts encapsulated in ultrathin 2D ZIF-67 layers using RDE in acidic solution. The Pt NPs encapsulated in ultrathin 2D ZIF-67 layers clearly show better HER activities than the Pt/C and Pt/RGO catalysts in acidic solution (Figure 4a). At a current density of  $10 \text{ mA cm}^{-2}$ , the 3ZIF-67-Pt/RGO has the lowest overpotential of  $14.3 \text{ mV}$  while 1ZIF-67-Pt/RGO and 5ZIF-67-Pt/RGO showed overpotentials of  $18.2 \text{ mV}$  and  $16.5 \text{ mV}$ , respectively, which are much lower than those of commercial Pt/C ( $23.1 \text{ mV}$ ) and Pt/RGO ( $29.0 \text{ mV}$ ) catalysts at the same Pt loading (Figure 4b). In addition, 3ZIF-67-Pt/RGO showed better HER activity than the PtCo alloy prepared by a wet method (Figure S12a). Tafel plots and electrochemical impedance spectroscopy (EIS) were further used to gain insight into the high HER catalytic performance of 3ZIF-67-Pt/RGO. The 3ZIF-67-Pt/RGO has the smallest

Tafel slope of  $12.5 \text{ mV dec}^{-1}$  (Figure S11a), which is lower than those of 5ZIF-67-Pt/RGO ( $13.6 \text{ mV dec}^{-1}$ ), 1ZIF-67-Pt/RGO ( $13.7 \text{ mV dec}^{-1}$ ), Pt/C ( $17.3 \text{ mV dec}^{-1}$ ), and Pt/RGO ( $18.2 \text{ mV dec}^{-1}$ ) catalysts, displaying a more favorable HER catalytic kinetics on the 3ZIF-67-Pt/RGO in acidic solution. As displayed in Figure S11b, the 3ZIF-67-Pt/RGO was observed to have the smallest charge transfer resistance among all samples, indicating that 3ZIF-67-Pt/RGO possesses a stronger charge transfer ability during the HER process in acid electrolytes. ADT were adopted to evaluate the durability of the as-prepared catalysts. The 3ZIF-67-Pt/RGO demonstrated significantly higher HER stability than the commercial Pt/C (Figure 4c and Figure S12b).

We further studied the HER activity of as-prepared catalysts in alkaline media, which is a major challenge for Pt catalysts because the alkaline HER activity of Pt catalysts is about two to three orders of magnitude lower than that in acidic media.<sup>57</sup> As shown in the Figure 4d,e, the Pt/C catalyst shows lower HER

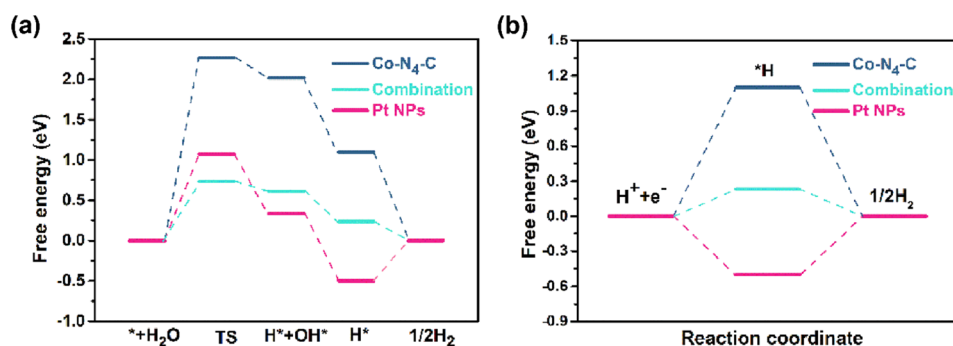


**Figure 5.** Calculated free-energy diagram of the HER on different active sites. (a) In alkaline and (b) in acidic media. Here, TS represents a transition state of  $\text{H}_2\text{O}$  activation.

activity with an overpotential of 92.1 mV in the alkaline solution. It is surprising that the Pt NPs encapsulated in 2D ultrathin carbon layers derived from ZIF-67 indicate enhanced HER activity in alkaline media. The 3ZIF-67-Pt/RGO and SZIF-67-Pt/RGO catalysts show overpotentials of 37.2 mV and 48.4 mV, respectively, which are much lower than that of commercial Pt/C (92.1 mV). The excellent HER activity on the 3ZIF-67-Pt/RGO sample is also reflected by the Tafel slope and EIS measurement in alkaline media, as shown in Figure S11c,d. The 3ZIF-67-Pt/RGO shows a lower Tafel slope and charge transfer resistance. In addition, 3ZIF-67-Pt/RGO also showed higher HER activity than the PtCo alloy prepared by a wet method (Figure S12c). After the durability tests, the 3ZIF-67-Pt/RGO retained a similar performance to the initial HER activity, demonstrating significantly higher HER stability compared with the commercial Pt/C in alkaline media (Figure 4f and Figure S12d). In addition, the carbonized ZIF-67 on GO without Pt NPs indicates low HER activity in acid and alkaline media (Figure S13). Those findings suggested the excellent catalytic activity and stability of 3ZIF-67-Pt/RGO in acid and alkaline media. The enhanced HER performance of 3ZIF-67-Pt/RGO is probably due to the unique structure of Pt encapsulated in ultrathin 2D carbon layers. The ultrathin 2D carbon protective layers derived from ZIF-67 are responsible for those remarkable improvements in the stability. The synergistic catalysis of Pt-based NPs and  $\text{Co-N}_4$ <sup>58–60</sup> derived from ZIF-67 can improve the HER activity in both acid and alkaline media.

We performed density functional theory (DFT) calculations to further understand the synergistic effects between the  $\text{Co-N}_x$  and Pt NPs during electrocatalysis of HER and ORR. It is reported that the  $\text{Co-N}_4$  derived from ZIF-67 has been widely recognized as active sites for ORR in both acidic and alkaline solutions.<sup>55,56</sup> Figure 5 presents the differences of Gibbs free energies of  $\text{Co-N}_4\text{-C}$ , Pt NPs, and the combination of  $\text{Co-N}_4\text{-C}$  and Pt NPs during the HER process in alkaline. It is observed that the energy barrier for the OH–H bond cleavage on  $\text{Co-N}_4\text{-C}$  and Pt NPs are 2.26 eV and 1.07 eV, respectively; whereas, the water dissociation energy barrier on the combination of  $\text{Co-N}_4\text{-C}$  and Pt NPs decreases to only 0.73 eV. The decrease in the dissociation energy barrier suggests that the combination of  $\text{Co-N}_4\text{-C}$  and Pt NPs can significantly accelerate the dissociation of water to  $\text{H}_{\text{ads}}$ , resulting in the fast kinetics of HER because the dissociation of water is the rate-limiting step of the HER in alkaline media. An ideal HER catalyst is expected to have a moderate hydrogen binding energy (HBE) in the step of the conversion of  $\text{H}^*$  to  $\text{H}_2$ , balancing the  $\text{H}^*$  adsorption and subsequent  $\text{H}_2$

desorption on the surface of catalysts.<sup>61</sup> The HBE values on  $\text{Co-N}_4\text{-C}$  and Pt NPs are 1.10 and 0.49 eV, respectively, much stronger than the optimal value (0 eV), resulting in the suppressing  $\text{H}^*$  desorption and subsequently hindering  $\text{H}_2$  generation. In contrast, the combination of  $\text{Co-N}_4\text{-C}$  and Pt NPs shows a more moderate HBE value of 0.23 eV, suggesting that the combination of  $\text{Co-N}_4\text{-C}$  and Pt NPs is a more efficient catalyst for the production of  $\text{H}_2$  than the  $\text{Co-N}_4\text{-C}$  and Pt NPs. Based on the above discussion, synergistic effects between the  $\text{Co-N}_4\text{-C}$  and Pt NPs can improve the HER activity in alkaline media through accelerating fast kinetics of HER by lowering the energy barrier for water dissociation and adjusting the HBE. In acidic media, compared with the  $\text{Co-N}_4\text{-C}$  and Pt NPs, the combination of  $\text{Co-N}_4$  and Pt NPs displays the lowest HBE of 0.23 eV, approaching the optimal value (0 eV), which facilitates the  $\text{H}^*$  adsorption and  $\text{H}_2$  desorption on the surface of the electrocatalysts and thereby leads to high HER activity. This finding indicates that the synergistic effects between the  $\text{Co-N}_4\text{-C}$  and Pt NPs also improve the HER activity in acidic media.

DFT calculations were also carried out to confirm the synergistic catalysis of Pt-based NPs and  $\text{Co-N}_4$  derived from ZIF-67 during the ORR process. In our calculation, the Pt-based NPs are idealized as Pt(111).<sup>53</sup> The detailed DFT calculations process for ORR is provided in the Supporting Information. As shown in Figure 6, the kinetic barrier for  $\text{OOH}^*$  formation on a  $\text{Co-N}_4$  site is only <0.1 eV, which is close to that of a Pt site. However, only on the  $\text{Co-N}_4\text{-C}$  active sites, it will form  $\text{O}^*$  and water and produce  $\text{H}_2\text{O}_2$  after the formation of  $^*\text{OOH}$ . When Pt(111) sites is in the vicinity of  $\text{Co-N}_4\text{-C}$  active sites, the  $\text{H}_2\text{O}_2$  generated on  $\text{Co-N}_4$  active sites can spillover to the adjacent Pt(111) sites to produce  $\text{H}_2\text{O}$  (Figure 6b). This finding suggests that the synergistic effects between the  $\text{Co-N}_4\text{-C}$  and Pt NPs can help the catalysis of  $\text{O}_2$  on the  $\text{Co-N}_4\text{-C}$  active sites to  $\text{H}_2\text{O}$  instead of  $\text{H}_2\text{O}_2$ .

### 3. CONCLUSIONS

In summary, we propose a facile approach to synthesize highly active and stable electrocatalysts by encapsulating Pt NPs with precisely controlled ultrathin carbon layers derived from the ultrathin 2D MOF precursor. The ultrathin 2D carbon layers not only provide suitable protecting layers for stabilizing Pt NPs but also introduce highly dispersed active sites. Our Pt catalysts encapsulated in ultrathin 2D carbon layers exhibited a higher stability with enhanced activity toward ORR and HER than commercial Pt/C catalysts. The enhanced performance of our encapsulated Pt catalysts are attributed to the synergistic

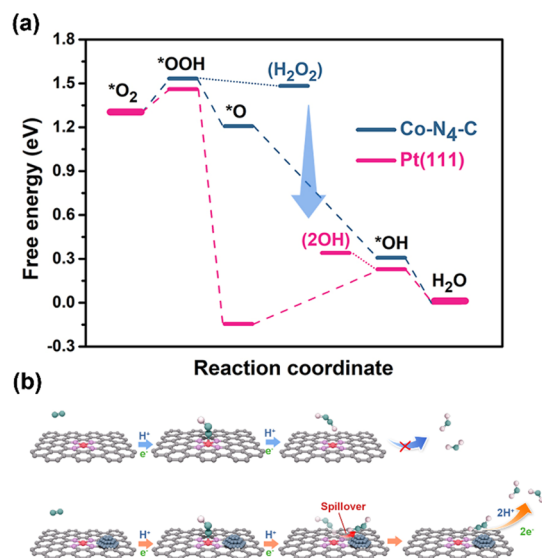


**Figure 6.** (a) Free-energy diagram of the ORR pathways. The blue line represents the Co-N<sub>4</sub>-C active site and pink line represents the Pt(111) active site. (b) Calculated structural model of the ORR pathways for Co-N<sub>4</sub>-C and the combination of Co-N<sub>4</sub>-C and Pt NPs.

effect of Pt-based NPs and ultrathin 2D carbon layers derived from ZIF-67 with enriched active sites Co-N<sub>x</sub>. First-principles simulations reveal that the synergistic catalysis of Pt-based NPs and Co-N<sub>4</sub> derived from ZIF-67 improves the activity for ORR and HER. The general synthetic approach presented in this work provides a promising candidate for the development of high-performance metal catalysts.

## 4. EXPERIMENTAL SECTION

**4.1. Synthesis of Pt/GO.** Graphene oxide was obtained by a modified Hummers method according to the previous study.<sup>41</sup> Pt/GO was synthesized as follows: Hexachloroplatinum(IV) acid (H<sub>2</sub>PtCl<sub>6</sub>·6H<sub>2</sub>O, 290 mg) was added to ethylene glycol (EG) and stirred for 0.5 h. The pH of the solution was adjusted to ~11 by addition of NaOH. Subsequently, the solution was heated to 200 °C in an oil bath and kept at this temperature for 3 h. After cooling down to room temperature, the EG solution containing 400 mg of graphene oxide was added to the black mixture to deposit Pt nanoparticles on GO. HCl was added to accelerate the deposition of Pt nanoparticles on GO. After stirring for 1 h, Pt/GO was obtained by centrifugation, washed several times with deionized water, and then freeze-dried.

**4.2. Synthesis of X-ZIF-67-Pt/GO.** Co(NO<sub>3</sub>)<sub>2</sub>·6H<sub>2</sub>O (800 mg) was dissolved in 400 mL of methanol solution containing 200 mg of Pt/GO and stirred for 1 hour. Pt/GO-adsorbed Co ions were obtained by centrifugation and washed with ethanol. Then, Pt/GO-adsorbed Co ions were dissolved again in 400 mL of methanol containing 2-methylimidazole (800 mg). After stirring for 1 h, the sample was acquired by centrifugation and washed with ethanol. The obtained sample was recorded as 1ZIF-67-Pt/GO. Samples 3ZIF-67-Pt/GO and 5ZIF-67-Pt/GO were obtained after repeating the above procedure three times and five times, respectively. The samples of X-ZIF-8-Pt/GO was prepared based on the above procedure with Zn(NO<sub>3</sub>)<sub>2</sub>·6H<sub>2</sub>O and 2-methylimidazole.

**4.3. Synthesis of Pt/RGO.** A 200 mg sample of Pt/GO in a quartz boat was heat-treated at 600 °C for 3 h under an N<sub>2</sub> atmosphere, and the sample Pt/RGO was obtained. The Pt loading for Pt/RGO is 22.3 wt % by ICP.

**4.4. Synthesis of X-ZIF-67-Pt/RGO.** All the samples of X-ZIF-67-Pt/GO were placed in a quartz boat and heated to 600 °C in an N<sub>2</sub> atmosphere for 3 h. The carbonized material was acid-washed with 1 M HCl for 2 h to remove residual Co species. Finally, the material

was dried at 60 °C under a vacuum to achieve the X-ZIF-67-Pt/RGO. The Pt loadings for 1ZIF-67-Pt/RGO, 3ZIF-67-Pt/RGO, and 5ZIF-67-Pt/RGO are 20.3, 17.2, and 15.7 wt %, respectively, by ICP.

**4.5. Synthesis of PtCo/RGO.** Appropriate amounts of H<sub>2</sub>PtCl<sub>6</sub>·6H<sub>2</sub>O, CoCl<sub>2</sub>·6H<sub>2</sub>O, and GO were added to 150 mL of ethylene glycol and ultrasonicated for 1 h. The pH of the mixture was adjusted to ~10 using NaOH. The mixture was heat-treated at 160 °C for 3 h. PtCo/RGO was obtained by centrifugation, washed several times with deionized water, and then freeze-dried. Then, the sample was heated to 600 °C for 3 h at 10% H<sub>2</sub>/90% N<sub>2</sub> to obtain PtCo/RGO.

**4.6. Synthesis of 3ZIF-67/RGO.** Co(NO<sub>3</sub>)<sub>2</sub>·6H<sub>2</sub>O (800 mg) was added to 400 mL of methanol solution containing 200 mg of GO and stirred for 1 hour. GO-adsorbed Co ions were obtained by centrifugation and washed with ethanol. Then, the GO-adsorbed Co ions were dissolved again in 400 mL of methanol containing 2-methylimidazole (800 mg). After stirring for 1 h, the sample was obtained by centrifugation and washed with ethanol. Sample 3ZIF-67/GO was obtained after repeating the above procedure 3 times. Sample 3ZIF-67/GO were heated at 600 °C for 3 h in N<sub>2</sub> atmosphere. The carbonized material was then acid-washed with 1 M HCl for 2 h to remove residual Co species. Finally, the material was dried under a vacuum to obtain the 3-ZIF-67/RGO.

**4.7. Material Characterization.** The thickness of the samples was characterized using an atomic force microscope (AFM, Agilent 5500). Scanning electron microscopy (SEM) was performed on a SUPRA 55. Transmission electron microscopy (TEM) images and wide-angle X-ray diffraction (XRD) patterns were obtained on FEI TECNAL G2F2O and D-MAX 2200 VPC, respectively. The particle size distribution was determined by measuring more than 200 Pt nanoparticles using a Nano Measurer. X-ray photoelectron spectroscopy (XPS) characterization was performed by a K-Alpha. Inductively coupled plasma mass spectrometer (ICP-MS) (iCAP7000, Thermo Fisher Scientific) was used to determine the Pt loading.

**4.8. Electrochemical Characterization.** All electrochemical measurements were conducted in a three-compartment cell at room temperature on an Autolab electrochemical workstation. We used a platinum wire, Ag/AgCl electrode, a rotating disk electrode (RDE) as the counter, reference, and working electrodes, respectively. The potentials in this work were converted to RHE according to  $E_{\text{RHE}} = E_{\text{Ag/AgCl}} + 0.197 + 0.059 \times \text{pH}$ . The uniform catalyst ink was prepared by mixing 4 mg of catalyst powder and 2 mL of solution containing 990 μL of deionized water, 990 μL of isopropanol, and 20 μL of Nafion ionomer solution. The ink was then coated on RDE (0.196 cm<sup>2</sup>), and the mass loading of Pt was 20 μg·cm<sup>-2</sup>. Before measurements, a steady CV of the working electrode was first obtained by cycling at 0.05–1.2 V at 50 mV·s<sup>-1</sup> in a N<sub>2</sub>-saturated 0.5 M H<sub>2</sub>SO<sub>4</sub> solution. An oxygen reduction reaction (ORR) linear sweep voltammetry (LSV, 10 mV·s<sup>-1</sup>) was performed in O<sub>2</sub>-saturated 0.5 M H<sub>2</sub>SO<sub>4</sub>. The hydrogen evolution reaction (HER) test used a three-electrode cell in alkaline solution (1 M KOH, pH = 14) and acidic solution (0.5 M H<sub>2</sub>SO<sub>4</sub>, pH = 0). A graphite rod instead of a Pt wire was used as a counter electrode. For HER tests, the final Pt loading of all samples was 10 μg·cm<sup>-2</sup>. Note that all the HER LSV tests were 100% iR-compensated.

## ■ ASSOCIATED CONTENT

### Supporting Information

The Supporting Information is available free of charge at <https://pubs.acs.org/doi/10.1021/acsami.9b20781>.

Computational method and mechanistic discussion, AFM and additional TEM images, additional XPS spectra, additional polarization curves, additional EDS mapping, and calculated structural model (PDF)

## ■ AUTHOR INFORMATION

## Corresponding Authors

**Niancai Cheng** – College of Materials Science and Engineering and Key Laboratory of Eco-materials Advanced Technology, Fuzhou University, Fuzhou 350108, China; [orcid.org/0000-0002-6358-5515](https://orcid.org/0000-0002-6358-5515); Email: [niancaicheng@fzu.edu.cn](mailto:niancaicheng@fzu.edu.cn)

**Xueliang Sun** – Department of Mechanical and Materials Engineering, The University of Western Ontario, London, ON N6A 5B9, Canada; [orcid.org/0000-0003-0374-1245](https://orcid.org/0000-0003-0374-1245); Email: [xsun@eng.uwo.ca](mailto:xsun@eng.uwo.ca)

## Authors

**Wei Wu** – College of Materials Science and Engineering and Key Laboratory of Eco-materials Advanced Technology, Fuzhou University, Fuzhou 350108, China

**Zeyi Zhang** – College of Materials Science and Engineering and Key Laboratory of Eco-materials Advanced Technology, Fuzhou University, Fuzhou 350108, China

**Zhao Lei** – College of Materials Science and Engineering and Key Laboratory of Eco-materials Advanced Technology, Fuzhou University, Fuzhou 350108, China

**Xiaoyue Wang** – College of Materials Science and Engineering and Key Laboratory of Eco-materials Advanced Technology, Fuzhou University, Fuzhou 350108, China

**Yangyang Tan** – College of Materials Science and Engineering and Key Laboratory of Eco-materials Advanced Technology, Fuzhou University, Fuzhou 350108, China

Complete contact information is available at: <https://pubs.acs.org/10.1021/acsami.9b20781>

## Notes

The authors declare no competing financial interest.

## ■ ACKNOWLEDGMENTS

This work was supported by the National Natural Science Foundation of China (grant no. 21875039), Minjiang Professorship (XRC-1677), Fujian province's High Level Innovative and Entrepreneurial Talents (50012709), and the Open Project Program of the State Key Laboratory of Photocatalysis on Energy and Environment (grant no. SKLPEE-201814), Fuzhou University.

## ■ REFERENCES

- (1) Bing, Y.; Liu, H.; Zhang, L.; Ghosh, D.; Zhang, J. Nanostructured Pt-Alloy Electrocatalysts for PEM Fuel Cell Oxygen Reduction Reaction. *Chem. Soc. Rev.* **2010**, *39*, 2184–2202.
- (2) Cheng, N.; Stambula, S.; Wang, D.; Banis, M. N.; Liu, J.; Riese, A.; Xiao, B.; Li, R.; Sham, T. K.; Liu, L. M.; Botton, G. A.; Sun, X. Platinum Single-Atom and Cluster Catalysis of the Hydrogen Evolution Reaction. *Nat. Commun.* **2016**, *7*, 13638.
- (3) Zhao, Z.; Liu, H.; Gao, W.; Xue, W.; Liu, Z.; Huang, J.; Pan, X.; Huang, Y. Surface-Engineered PtNi-O Nanostructure with Record-High Performance for Electrocatalytic Hydrogen Evolution Reaction. *J. Am. Chem. Soc.* **2018**, *140*, 9046–9050.
- (4) Sun, H.; Yan, Z.; Liu, F.; Xu, W.; Cheng, F.; Chen, J. Self-Supported Transition-Metal-Based Electrocatalysts for Hydrogen and Oxygen Evolution. *Adv. Mater.* **2019**, *32*, 1806326.
- (5) Cheng, X.; Li, Y.; Zheng, L.; Yan, Y.; Zhang, Y.; Chen, G.; Sun, S.; Zhang, J. Highly Active, Stable Oxidized Platinum Clusters as Electrocatalysts for the Hydrogen Evolution Reaction. *Energy Environ. Sci.* **2017**, *10*, 2450–2458.
- (6) Zhang, Y.; Luo, M.; Yang, Y.; Li, Y.; Guo, S. Advanced Multifunctional Electrocatalysts for Energy Conversion. *ACS Energy Lett.* **2019**, *4*, 1672–1680.
- (7) Cheng, N.; Banis, M. N.; Liu, J.; Riese, A.; Mu, S.; Li, R.; Sham, T.-K.; Sun, X. Atomic Scale Enhancement of Metal-Support Interactions between Pt and ZrC for Highly Stable Electrocatalysts. *Energy Environ. Sci.* **2015**, *8*, 1450–1455.
- (8) Song, S.; Wang, X.; Zhang, H. CeO<sub>2</sub>-Encapsulated Noble Metal Nanocatalysts: Enhanced Activity and Stability for Catalytic Application. *NPG Asia Mater.* **2015**, *7*, e179.
- (9) Jiang, K.; Bu, L.; Wang, P.; Guo, S.; Huang, X. Trimetallic PtSnRh Wavy Nanowires as Efficient Nanoelectrocatalysts for Alcohol Electrooxidation. *ACS Appl. Mater. Interfaces* **2015**, *7*, 15061–15067.
- (10) Chung, D. Y.; Yoo, J. M.; Sung, Y.-E. Highly Durable and Active Pt-Based Nanoscale Design for Fuel-Cell Oxygen-Reduction Electrocatalysts. *Adv. Mater.* **2018**, *30*, 1704123.
- (11) Cheng, K.; Zhu, K.; Liu, S.; Li, M.; Huang, J.; Yu, L.; Xia, Z.; Zhu, C.; Liu, X.; Li, W.; Lu, W.; Wei, F.; Zhou, Y.; Zheng, W.; Mu, S. A Spatially Confined gC<sub>3</sub>N<sub>4</sub>-Pt Electrocatalyst with Robust Stability. *ACS Appl. Mater. Interfaces* **2018**, *10*, 21306–21312.
- (12) Kim, H.; Robertson, A. W.; Kim, S. O.; Kim, J. M.; Warner, J. H. Resilient High Catalytic Performance of Platinum Nanocatalysts with Porous Graphene Envelope. *ACS Nano* **2015**, *9*, 5947–5957.
- (13) Chung, D. Y.; Jun, S. W.; Yoon, G.; Kwon, S. G.; Shin, D. Y.; Seo, P.; Yoo, J. M.; Shin, H.; Chung, Y.-H.; Kim, H.; Mun, B. S.; Lee, K.-S.; Lee, N.-S.; Yoo, S. J.; Lim, D.-H.; Kang, K.; Sung, Y.-E.; Hyeon, T. Highly Durable and Active PtFe Nanocatalyst for Electrochemical Oxygen Reduction Reaction. *J. Am. Chem. Soc.* **2015**, *137*, 15478–15485.
- (14) Deng, J.; Ren, P.; Deng, D.; Bao, X. Enhanced Electron Penetration through an Ultrathin Graphene Layer for Highly Efficient Catalysis of the Hydrogen Evolution Reaction. *Angew. Chem., Int. Ed.* **2015**, *54*, 2100–2104.
- (15) Cheng, N.; Banis, M. N.; Liu, J.; Riese, A.; Li, X.; Li, R.; Ye, S.; Knights, S.; Sun, X. Extremely Stable Platinum Nanoparticles Encapsulated in a Zirconia Nanocage by Area-Selective Atomic Layer Deposition for the Oxygen Reduction Reaction. *Adv. Mater.* **2015**, *27*, 277–281.
- (16) Lu, J.; Fu, B.; Kung, M. C.; Xiao, G.; Elam, J. W.; Kung, H. H.; Stair, P. C. Coking- and Sintering-Resistant Palladium Catalysts Achieved through Atomic Layer Deposition. *Science* **2012**, *335*, 1205–1208.
- (17) Takenaka, S.; Miyamoto, H.; Utsunomiya, Y.; Matsune, H.; Kishida, M. Catalytic Activity of Highly Durable Pt/CNT Catalysts Covered with Hydrophobic Silica Layers for the Oxygen Reduction Reaction in PEFCs. *J. Phys. Chem. C* **2014**, *118*, 774–783.
- (18) Cheng, N.; Mu, S.; Pan, M.; Edwards, P. P. Improved Lifetime of PEM Fuel Cell Catalysts through Polymer Stabilization. *Electrochem. Commun.* **2009**, *11*, 1610–1614.
- (19) Chen, S.; Wei, Z.; Qi, X.; Dong, L.; Guo, Y.-G.; Wan, L.; Shao, Z.; Li, L. Nanostructured Polyaniline-Decorated Pt/C@PANI Core-Shell Catalyst with Enhanced Durability and Activity. *J. Am. Chem. Soc.* **2012**, *134*, 13252–13255.
- (20) Cheng, K.; Kou, Z.; Zhang, J.; Jiang, M.; Wu, H.; Hu, L.; Yang, X.; Pan, M.; Mu, S. Ultrathin Carbon Layer Stabilized Metal Catalysts towards Oxygen Reduction. *J. Mater. Chem. A* **2015**, *3*, 14007–14014.
- (21) Baldizzone, C.; Mezzavilla, S.; Carvalho, H. W. P.; Meier, J. C.; Schuppert, A. K.; Heggen, M.; Galeano, C.; Grunwaldt, J.-D.; Schüth, F.; Mayrhofer, K. J. J. Confined-Space Alloying of Nanoparticles for the Synthesis of Efficient PtNi Fuel-Cell Catalysts. *Angew. Chem., Int. Ed.* **2014**, *53*, 14250–14254.
- (22) Ren, G.; Lu, X.; Li, Y.; Zhu, Y.; Dai, L.; Jiang, L. Porous Core-Shell Fe<sub>3</sub>C Embedded N-Doped Carbon Nanofibers as an Effective Electrocatalysts for Oxygen Reduction Reaction. *ACS Appl. Mater. Interfaces* **2016**, *8*, 4118–4125.
- (23) Liu, J.; Li, W.; Cheng, R.; Wu, Q.; Zhao, J.; He, D.; Mu, S. Stabilizing Pt Nanocrystals Encapsulated in N-Doped Carbon as Double-Active Sites for Catalyzing Oxygen Reduction Reaction. *Langmuir* **2019**, *35*, 2580–2586.
- (24) Tong, X.; Zhang, J.; Zhang, G.; Wei, Q.; Chenitz, R.; Claverie, J. P.; Sun, S. Ultrathin Carbon-Coated Pt/Carbon Nanotubes: A

Highly Durable Electrocatalyst for Oxygen Reduction. *Chem. Mater.* **2017**, *29*, 9579–9587.

(25) Gao, Z.; Qin, Y. Design and Properties of Confined Nanocatalysts by Atomic Layer Deposition. *Acc. Chem. Res.* **2017**, *50*, 2309–2316.

(26) Takenaka, S.; Miyazaki, T.; Matsune, H.; Kishida, M. Highly Active and Durable Silica-Coated Pt Cathode Catalysts for Polymer Electrolyte Fuel Cells: Control of Micropore Structures in Silica Layers. *Catal. Sci. Technol.* **2015**, *5*, 1133–1142.

(27) Lu, P.; Campbell, C. T.; Xia, Y. A Sinter-Resistant Catalytic System Fabricated by Maneuvering the Selectivity of SiO<sub>2</sub> Deposition onto the TiO<sub>2</sub> Surface versus the Pt Nanoparticle Surface. *Nano Lett.* **2013**, *13*, 4957–4962.

(28) Ray, N. A.; Van Duyne, R. P.; Stair, P. C. Synthesis Strategy for Protected Metal Nanoparticles. *J. Phys. Chem. C* **2012**, *116*, 7748–7756.

(29) Liu, X.; Zhu, Q.; Lang, Y.; Cao, K.; Chu, S.; Shan, B.; Chen, R. Oxide-Nanotrap-Anchored Platinum Nanoparticles with High Activity and Sintering Resistance by Area-Selective Atomic Layer Deposition. *Angew. Chem., Int. Ed.* **2017**, *56*, 1648–1652.

(30) Li, G.; Zhao, S.; Zhang, Y.; Tang, Z. Metal-Organic Frameworks Encapsulating Active Nanoparticles as Emerging Composites for Catalysis: Recent Progress and Perspectives. *Adv. Mater.* **2018**, *30*, 1800702.

(31) Du, N.; Wang, C.; Long, R.; Xiong, Y. N-doped Carbon-Stabilized PtCo Nanoparticles Derived from Pt@ZIF-67: Highly Active and Durable Catalysts for Oxygen Reduction Reaction. *Nano Res.* **2017**, *10*, 3228–3237.

(32) Jin, S. How to Effectively Utilize MOFs for Electrocatalysis. *ACS Energy Lett.* **2019**, *4*, 1443–1445.

(33) Hu, P.; Zhuang, J.; Chou, L. Y.; Lee, H. K.; Ling, X. Y.; Chuang, Y. C.; Tsung, C. K. Surfactant-Directed Atomic to Mesoscale Alignment: Metal Nanocrystals Encased Individually in Single-Crystalline Porous Nanostructures. *J. Am. Chem. Soc.* **2014**, *136*, 10561–10564.

(34) Rungtaweeworant, B.; Baek, J.; Araujo, J. R.; Archanjo, B. S.; Choi, K. M.; Yaghi, O. M.; Somorjai, G. A. Copper Nanocrystals Encapsulated in Zr-based Metal-Organic Frameworks for Highly Selective CO<sub>2</sub> Hydrogenation to Methanol. *Nano Lett.* **2016**, *16*, 7645–7649.

(35) Yang, Q.; Xu, Q.; Jiang, H.-L. Metal-Organic Frameworks Meet Metal Nanoparticles: Synergistic Effect for Enhanced Catalysis. *Chem. Soc. Rev.* **2017**, *46*, 4774–4808.

(36) Wu, Z.; Guo, J.; Wang, J.; Liu, R.; Xiao, W.; Xuan, C.; Xia, K.; Wang, D. Hierarchically Porous Electrocatalyst with Vertically Aligned Defect-Rich CoMoS Nanosheets for the Hydrogen Evolution Reaction in an Alkaline Medium. *ACS Appl. Mater. Interfaces* **2017**, *9*, 5288–5294.

(37) Shekhah, O.; Wang, H.; Kowarik, S.; Schreiber, F.; Paulus, M.; Tolan, M.; Sternemann, C.; Evers, F.; Zacher, D.; Fischer, R. A.; Wöll, C. Step-by-Step Route for the Synthesis of Metal–Organic Frameworks. *J. Am. Chem. Soc.* **2007**, *129*, 15118–15119.

(38) Zhao, G.; Li, J.; Ren, X.; Chen, C.; Wang, X. Few-Layered Graphene Oxide Nanosheets as Superior Sorbents for Heavy Metal Ion Pollution Management. *Environ. Sci. Technol.* **2011**, *45*, 10454–10462.

(39) Fang, F.; Kong, L.; Huang, J.; Wu, S.; Zhang, K.; Wang, X.; Sun, B.; Jin, Z.; Wang, J.; Huang, X. J.; Liu, J. Removal of Cobalt Ions from Aqueous Solution by an Amination Graphene Oxide Nanocomposite. *J. Hazard. Mater.* **2014**, *270*, 1–10.

(40) Cheng, N.; Mu, S.; Chen, X.; Lv, H.; Pan, M.; Edwards, P. P. Enhanced Life of Proton Exchange Membrane Fuel Cell Catalysts Using Perfluorosulfonic Acid Stabilized Carbon Support. *Electrochim. Acta* **2011**, *56*, 2154–2159.

(41) Cheng, N.; Liu, J.; Banis, M. N.; Geng, D.; Li, R.; Ye, S.; Knights, S.; Sun, X. High Stability and Activity of Pt Electrocatalyst on Atomic Layer Deposited Metal Oxide/Nitrogen-Doped Graphene Hybrid Support. *Int. J. Hydrogen Energy* **2014**, *39*, 15967–15974.

(42) Qi, Z.; Xiao, C.; Liu, C.; Goh, T. W.; Zhou, L.; Maligal-Ganesh, R.; Pei, Y.; Li, X.; Curtiss, L. A.; Huang, W. Sub-4 nm PtZn Intermetallic Nanoparticles for Enhanced Mass and Specific Activities in Catalytic Electrooxidation Reaction. *J. Am. Chem. Soc.* **2017**, *139*, 4762–4768.

(43) Xia, B. Y.; Wu, H. B.; Li, N.; Yan, Y.; Lou, X. W. D.; Wang, X. One-Pot Synthesis of Pt-Co Alloy Nanowire Assemblies with Tunable Composition and Enhanced Electrocatalytic Properties. *Angew. Chem., Int. Ed.* **2015**, *54*, 3797–3801.

(44) Qi, Z.; Pei, Y.; Goh, T. W.; Wang, Z.; Li, X.; Lowe, M.; Maligal-Ganesh, R. V.; Huang, W. Conversion of Confined Metal@ZIF-8 Structures to Intermetallic Nanoparticles Supported on Nitrogen-Doped Carbon for Electrocatalysis. *Nano Res.* **2018**, *11*, 3469–3479.

(45) Wang, D.; Xin, H. L.; Hovden, R.; Wang, H.; Yu, Y.; Muller, D. A.; DiSalvo, F. J.; Abruña, H. D. Structurally Ordered Intermetallic Platinum-Cobalt Core-Shell Nanoparticles with Enhanced Activity and Stability as Oxygen Reduction Electrocatalysts. *Nat. Mater.* **2013**, *12*, 81–87.

(46) Wang, X. X.; Hwang, S.; Pan, Y. T.; Chen, K.; He, Y.; Karakalos, S.; Zhang, H.; Spindel, J. S.; Su, D.; Wu, G. Ordered Pt<sub>3</sub>Co Intermetallic Nanoparticles Derived from Metal-Organic Frameworks for Oxygen Reduction. *Nano Lett.* **2018**, *18*, 4163–4171.

(47) Wang, T.; Liang, J.; Zhao, Z.; Li, S.; Lu, G.; Xia, Z.; Wang, C.; Luo, J.; Han, J.; Ma, C.; Huang, Y.; Li, Q. Sub-6 nm Fully Ordered L10-Pt-Ni-Co Nanoparticles Enhance Oxygen Reduction via Co Doping Induced Ferromagnetism Enhancement and Optimized Surface Strain. *Adv. Energy Mater.* **2019**, *9*, 1803771.

(48) Park, H.; Oh, S.; Lee, S.; Choi, S.; Oh, M. Cobalt- and Nitrogen-Codoped Porous Carbon Catalyst Made from Core-Shell Type Hybrid Metal–Organic Framework (ZIF-L@ZIF-67) and Its Efficient Oxygen Reduction Reaction (ORR) Activity. *Appl. Catal., B* **2019**, *246*, 322–329.

(49) Cheng, Q.; Han, S.; Mao, K.; Chen, C.; Yang, L.; Zou, Z.; Gu, M.; Hu, Z.; Yang, H. Co Nanoparticle Embedded in Atomically-Dispersed Co-N-C Nanofibers for Oxygen Reduction with High Activity and Remarkable Durability. *Nano Energy* **2018**, *52*, 485–493.

(50) Zhang, W.; Yao, X.; Zhou, S.; Li, X.; Li, L.; Yu, Z.; Gu, L. ZIF-8/ZIF-67-Derived Co-Nx-Embedded 1D Porous Carbon Nanofibers with Graphitic Carbon-Encased Co Nanoparticles as an Efficient Bifunctional Electrocatalyst. *Small* **2018**, *14*, 1800423.

(51) Yu, P.; Wang, L.; Sun, F.; Xie, Y.; Liu, X.; Ma, J.; Wang, X.; Tian, C.; Li, J.; Fu, H. Co Nanosheets Rooted on Co–N–C Nanosheets as Efficient Oxygen Electrocatalyst for Zn–Air Batteries. *Adv. Mater.* **2019**, *31*, 1901666.

(52) Bai, L.; Liu, J.; Gu, W.; Song, Y.; Wang, F. Carbon-Based Nanostructures Vertically Arrayed on Layered Lanthanum Oxycarbonate as Highly Efficient Catalysts for Oxygen Reduction Reactions. *ACS Appl. Mater. Interfaces* **2019**, *11*, 16452–16460.

(53) Chong, L.; Wen, J.; Kubal, J.; Sen, F. G.; Zou, J.; Greeley, J.; Chan, M.; Barkholtz, H.; Ding, W.; Liu, D. J. Ultralow-Loading Platinum-Cobalt Fuel Cell Catalysts Derived from Imidazolite Frameworks. *Science* **2018**, *362*, 1276–1281.

(54) Liu, J.; Zhu, D.; Guo, C.; Vasileff, A.; Qiao, S.-Z. Design Strategies toward Advanced MOF-Derived Electrocatalysts for Energy-Conversion Reactions. *Adv. Energy Mater.* **2017**, *7*, 1700518.

(55) Wang, X.; Zhou, J.; Fu, H.; Li, W.; Fan, X.; Xin, G.; Zheng, J.; Li, X. MOF Derived Catalysts for Electrochemical Oxygen Reduction. *J. Mater. Chem. A* **2014**, *2*, 14064–14070.

(56) Yin, P.; Yao, T.; Wu, Y.; Zheng, L.; Lin, Y.; Liu, W.; Ju, H.; Zhu, J.; Hong, X.; Deng, Z.; Zhou, G.; Wei, S.; Li, Y. Single Cobalt Atoms with Precise N-Coordination as Superior Oxygen Reduction Reaction Catalysts. *Angew. Chem., Int. Ed.* **2016**, *55*, 10800–10805.

(57) Pu, Z.; Amiin, I. S.; Kou, Z.; Li, W.; Mu, S. RuP<sub>2</sub>-Based Catalysts with Platinum-like Activity and Higher Durability for the Hydrogen Evolution Reaction at All pH Values. *Angew. Chem., Int. Ed. Engl.* **2017**, *56*, 11559–11564.

(58) Zhang, L.; Xiao, J.; Wang, H.; Shao, M. Carbon-Based Electrocatalysts for Hydrogen and Oxygen Evolution Reactions. *ACS Catal.* **2017**, *7*, 7855–7865.

(59) Wang, Z.-L.; Hao, X.-F.; Jiang, Z.; Sun, X.-P.; Xu, D.; Wang, J.; Zhong, H.-X.; Meng, F.-L.; Zhang, X.-B. C and N Hybrid Coordination Derived Co–C–N Complex as a Highly Efficient Electrocatalyst for Hydrogen Evolution Reaction. *J. Am. Chem. Soc.* **2015**, *137*, 15070–15073.

(60) Morozan, A.; Goellner, V.; Nedellec, Y.; Hannauer, J.; Jaouen, F. Effect of the Transition Metal on Metal–Nitrogen–Carbon Catalysts for the Hydrogen Evolution Reaction. *J. Electrochem. Soc.* **2015**, *162*, H719–H726.

(61) Nørskov, J. K.; Bligaard, T.; Logadottir, A.; Kitchin, J. R.; Chen, J. G.; Pandelov, S.; Stimming, U. Trends in the Exchange Current for Hydrogen Evolution. *J. Electrochem. Soc.* **2005**, *152*, J23–J26.